

From convection rolls to finger convection in double-diffusive turbulence

Yantao Yang

*Physics of Fluids Group, MESA+ Research Institute,
and J. M. Burgers Centre for Fluid Dynamics,
University of Twente, PO Box 217,
7500 AE Enschede, The Netherlands.*

Roberto Verzicco

*Physics of Fluids Group, MESA+ Research Institute,
and J. M. Burgers Centre for Fluid Dynamics,
University of Twente, PO Box 217,
7500 AE Enschede, The Netherlands. and
Dipartimento di Ingegneria Industriale,
University of Rome “Tor Vergata”,
Via del Politecnico 1, Roma 00133, Italy*

Detlef Lohse

*Physics of Fluids Group, MESA+ Research Institute,
and J. M. Burgers Centre for Fluid Dynamics,
University of Twente, PO Box 217,
7500 AE Enschede, The Netherlands. and
Max-Planck Institute for Dynamics and Self-Organization,
Am Fassberg 17, 37077 Göttingen, Germany.*

(Dated: November 18, 2015)

Abstract

Double diffusive convection (DDC), which is the buoyancy driven flow with fluid density depending on two scalar components, is ubiquitous in many natural and engineering environments. Of great interests are scalars transfer rate and flow structures. Here we systematically investigate DDC flow between two horizontal plates, driven by an unstable salinity gradient and stabilized by a temperature gradient. Counterintuitively, when increasing the stabilizing temperature gradient, the salinity flux first increases, even though the velocity monotonically decreases, before it finally breaks down to the purely diffusive value. The enhanced salinity transport is traced back to a transition in the overall flow pattern, namely from large scale convection rolls to well-organised vertically-oriented salt fingers. We also show and explain that the unifying theory of thermal convection originally developed by Grossmann and Lohse for Rayleigh-Bénard convection can be directly applied to DDC flow for a wide range of control parameters (Lewis number and density ratio), including those which cover the common values relevant for ocean flows.

Double diffusive convection (DDC), where the flow density depends on two scalar components, is of great relevance in many natural phenomena and engineering applications, such as oceanography [1–3], geophysics [4, 5], astrophysics [6–10], and process technology [11]. A comprehensive review of the field can be found in the recent book of Ref. [17]. In DDC flows the two components usually have very different molecular diffusivities. For simplicity and to take the most relevant example, we refer to the fast diffusing scalar as temperature and the other as salinity, but our results are more general. The difference between the diffusing time scales of two components induces interesting flow phenomena, such as the well-known salt fingers observed in ocean flows [3, 18].

In laboratory experiments salt fingers can grow from a sharp interface [19] or inside a layer which has uniform scalar gradients and is bounded by two reservoirs [20, 21]. For the latter case a single finger layer or a stack of alternating finger and convection layers was observed for different control parameters. Inside the finger layers long narrow salt fingers develop vertically, while in convection layer fluid is well mixed by large scale circulation. Recent experiments [22] revealed that fingers emerge even when the density ratio, i.e., the ratio of the buoyancy force induced by temperature gradient to that by salinity gradient, is smaller than 1. This extends the traditional finger regime where the density ratio is usually larger than 1, and inspired a reexamination of the salt-finger theory which confirmed that salt fingers do grow in this new finger regime [23]. When the density ratio is small enough, however, finger convection breaks down and gives way to large scale convection rolls, i.e. the flow recovers the Rayleigh-Bénard (RB) type [24].

Given the ubiquitousness of DDC in diverse circumstances, it is challenging to experimentally investigate the problem for a wide range of control parameters. Here we conduct a systematic numerical study of DDC flow between two parallel plates which are perpendicular to gravity and separated by a distance L . The details of the numerical method is briefly described in the Method section. The top plate has both higher salinity and temperature, meaning that the flow is driven by the salinity difference Δ_S across the layer and stabilised by temperature difference Δ_T . The molecular diffusivity λ_ζ of a scalar component is usually measured by its ratio to the kinematic viscosity ν , i.e. the Prandtl number $Pr_\zeta = \nu/\lambda_\zeta$. Hereafter $\zeta = T$ or S denotes the quantity related to temperature or salinity. The strength of the driving force is measured by the Rayleigh number $Ra_\zeta = (g\beta_\zeta\Delta_\zeta L^3)/(\lambda_\zeta\nu)$ with g being the gravitational acceleration and β_ζ the positive expansion coefficient. The relative strength of

the buoyancy force induced by temperature difference compared to that induced by salinity difference is measured by density ratio defined as $\Lambda = (\beta_T \Delta_T)/(\beta_S \Delta_S) = Le Ra_T Ra_S^{-1}$. When $\Lambda = 0$ the flow is of RB type and purely driven by the salinity difference. $\Lambda < 1$ (> 1) corresponds to an overall unstable (stable) stratification. Linear stability analysis revealed that instabilities occur as long as $\Lambda < Le$ [18]. As we will show below, the direct numerical simulations of the fully non-linear system indicate that flows develop in the same parameter range, i.e. $\Lambda < Le$.

Previous experiments with a heat-copper-ion system [24] showed that as Le increases from zero, the flow transits from large convective rolls to salt fingers, which is accompanied by an increase of the salinity transfer. However, the experiments were conducted with a single type of fluid and thus only one combination of Prandtl numbers was investigated. Moreover, the highest density ratio realised in experiments was of order 1. In the present study we will take advantage of numerical simulations which can be easily carried out for a wide range of Prandtl numbers and allow for a more systematic investigation of the problem. We set $Pr_T = 7$, which is the typical value for seawater at 20 °C. Several sets of simulations are conducted with different Pr_S and Ra_S . Since Pr_T is fixed for all simulations, we can alternatively use the Lewis number $Le = \lambda_T/\lambda_S = Pr_S/Pr_T$ and Ra_S to label different sets. Specifically, we run five sets with $(Le, Ra_S) = (1, 10^8)$, $(10, 10^8)$, $(100, 10^7)$, $(100, 10^8)$, and $(100, 10^9)$, respectively. Within each set we gradually increase Λ from 0 (i.e. RB flow) to a value very close to Le .

In Fig. 1 we show the typical flow structures observed in our simulations. For $Le = 1$, even with Λ up to 0.1 as shown in Fig. 1a the flow structures are very similar to those in the RB case. Near boundaries sheet structures emerge as the roots of salt plumes, e.g. see the contours on two slices at $z = 0.04$ and 0.96 in Fig. 1a. These sheet structures gather in some regions, from where the salt plumes emit into the bulk as clusters. The plume clusters move collectively and drive the large-scale convection rolls. When $Le > 1$, flow structures are of RB type at small Λ , as shown in Fig. 1b. The flow morphology is essentially the same as in Fig. 1a, i.e. the salt plumes still form clusters and drive the large scale rolls. The salt plumes become thinner and more circular due to the larger Pr_S than that in Fig. 1a. At moderate $\Lambda = 1.0$, however, the salt plumes stop gathering and convection rolls are replaced by vertically-oriented salt fingers. The highly organising pattern can be found both in the sheet structures near plates and the salt fingers in the middle, as indicated by contours on

three slices shown in Fig. 1c. These well-organised fingers develop separately and extend from one plate to the opposite one. When Λ increases close to Le , all flow motions are suppressed by the strong temperature field for all Le 's considered here.

Based on the flow morphology observed in simulations, different flow regimes can be identified. In Fig. 2 we present the explored control parameters and a schematic division of phase space into three regimes based on the numerical observations. The three sets with the same Ra_S and different Le are shown in the Λ - Le phase plane, see Fig. 2a. For very small density ratio the flow is dominated by large-scale convection rolls, which we refer to as the quasi-RB regime. When Λ is very close to Le all flow motions start to be suppressed by the strong temperature field, which we refer to as the damping regime. When $Le = 1$ the flow directly transits from the quasi-RB regime into the damping regime as Λ increases. For $Le > 1$ salt fingers develop at moderate Λ and a finger regime can be identified. As Le increases the finger regime occupies a wider range of Λ . The transition point between the quasi-RB and the finger regime for the heat-copper-ion system has been experimentally determined at $(\Lambda, Le) \approx (226, 1/30)$ [24], which is also marked in Fig. 2a, and it is very close to the transition boundary found in the current study. For fixed $Le = 100$, the transition between regimes happens at similar Λ for different Ra_S . Similar behaviour of the transition between the quasi-RB and finger regimes has been discovered experimentally for $Le \approx 226$ [24], i.e. the transition is independent of Ra_S . However, in the experiment the highest density ratio is of order 1 and therefore only the quasi-RB and finger regimes were identified [24].

In Ref. [24] the authors proposed two possible scaling laws to describe the transition between the quasi-RB and finger regimes, i.e. $\Lambda = const.$ or $Ra_T \sim Pr_T^{6/7} Ra_S^{22/21}$. The latter one is equivalent to $\Lambda \sim Pr_T^{6/7} Ra_S^{1/21} Le$. Since all of their experiments have similar Pr_T and Le , the only difference between the two possibilities is the factor $Ra_S^{1/21}$ with an exponent too small to be distinguished by the experimental measurement. However, the two scalings have different dependences on Le , which can be tested against our numerical results. From Fig. 2a one observes that as Le increases the transition to the finger regime happens at smaller Λ , which contradicts the second scaling. However, the current results are compatible with the first scaling.

Different flow structures have significant influences on the global responses of system. The two most important responses are the salinity flux and the flow velocity, which are

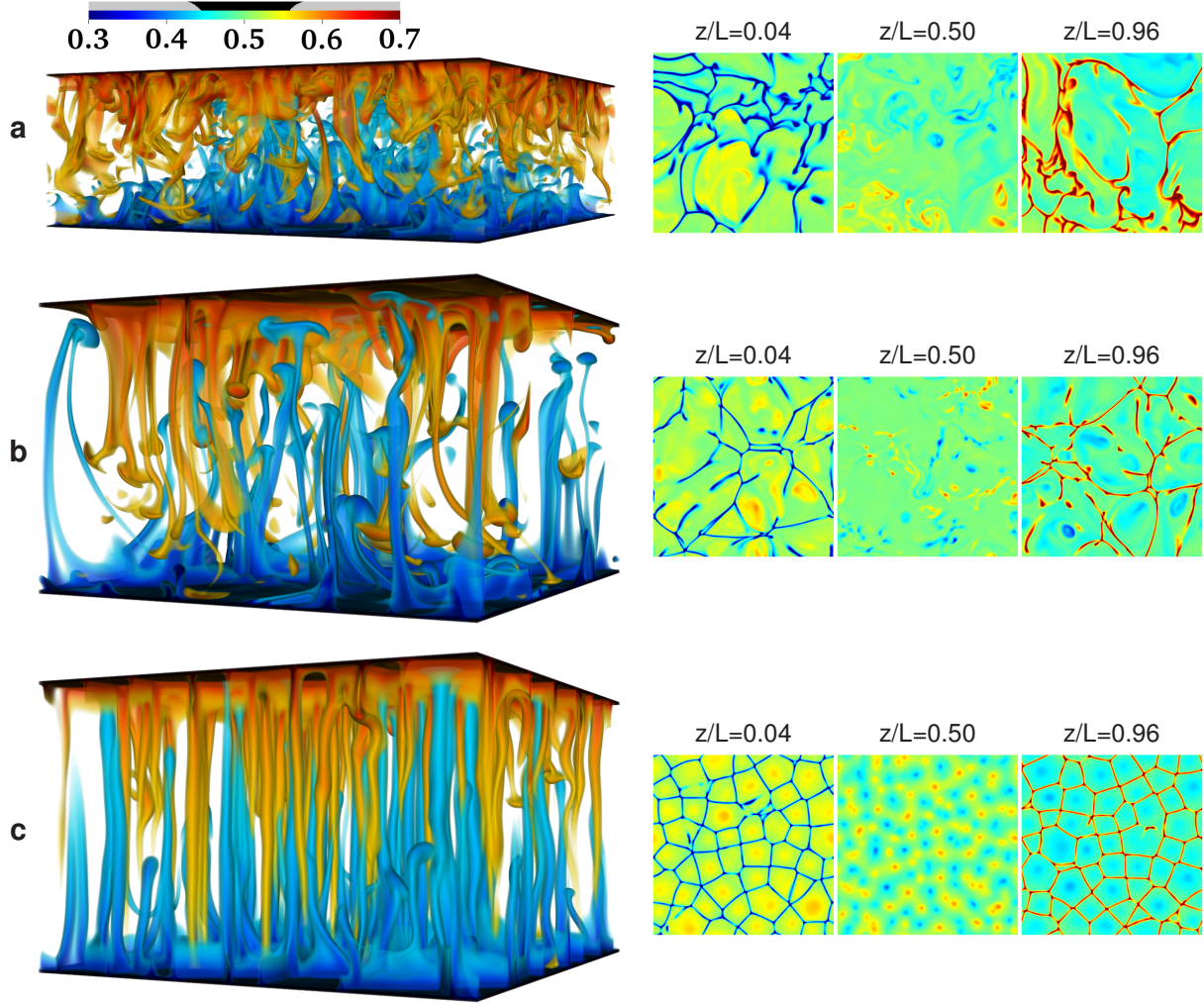


FIG. 1. Different types of flow structures observed in simulations with (a) $(Le, \Lambda) = (1, 0.1)$, (b) $(Le, \Lambda) = (100, 10^{-3})$, and (c) $(Le, \Lambda) = (100, 1)$. For all three cases $Ra_S = 10^8$. We show the three dimensional (3D) rendering of structures with low (blue) and high (red) salinity, and salinity contours on three horizontal slices at different heights. The same colormap is used for all plots. In the 3D plots the opacity is also set by salinity, as indicated by the legend. In (a) the plumes gather into clusters and move collectively in vertical direction, which drives the large scale convection rolls. In (b) the plumes becomes thinner due to the larger Pr_S , but they still form clusters and large scale convection rolls. In (c) the large-scale rolls are replaced by well-organised vertically-oriented salinity fingers, which extend through the entire domain heights. In all 3D plots the saltier and fresher plumes (or fingers) develop from top and bottom plates, respectively.

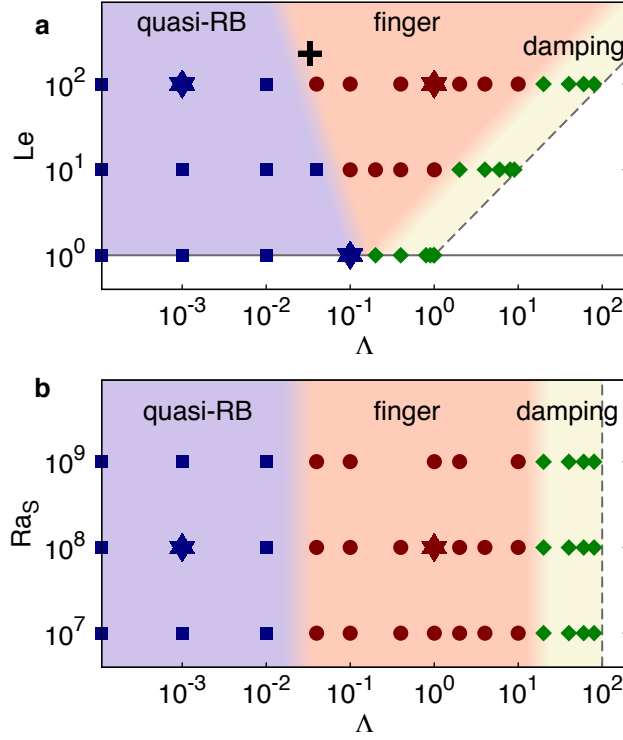


FIG. 2. Explored phase space and schematic illustration of different flow regimes. (a) The three sets of simulations with $Ra_S = 10^8$ are shown in the $\Lambda - Le$ plane, and (b) the three sets with $Le = 100$ are shown in the $\Lambda - Ra_S$ plane, respectively. The top row in (a) and the middle row in (b) correspond to the same set of simulations. The horizontal solid line in (a) marks $Le = 1$, below which the flow enters the diffusive regime of DDC, i.e. the fast diffusing component drives the flow. The dashed lines in both panels represent the stability limit $\Lambda = Le$. Three flow regimes can be identified and indicated by different colours: The quasi-RB regime (blue), the finger regime (orange), and the damping regime (grey). The three stars in (a) and two stars in (b) mark the cases shown in Fig. 1. The black plus sign in (a) indicate the transition point reported in Ref. [24].

usually measured by the Nusselt number Nu_S and the Reynolds number Re_a .

$$Nu_S = \frac{\langle u_3 s \rangle - \lambda_S \partial_3 \langle s \rangle}{\lambda_S \Delta_S L^{-1}}, \quad Re_a = \frac{u_{rms} L}{\nu}. \quad (1)$$

Here u_3 is vertical velocity, s is salinity, ∂_3 is vertical derivative, $\langle \cdot \rangle$ is the average over time and the entire domain, and u_{rms} is the rms value of velocity magnitude, respectively. In Fig. 3 we plot the variations of Nu_S and Re_a normalized by the values of corresponding RB flow (denoted by superscript “RB”) as Λ increases from zero to Le . The two quantities

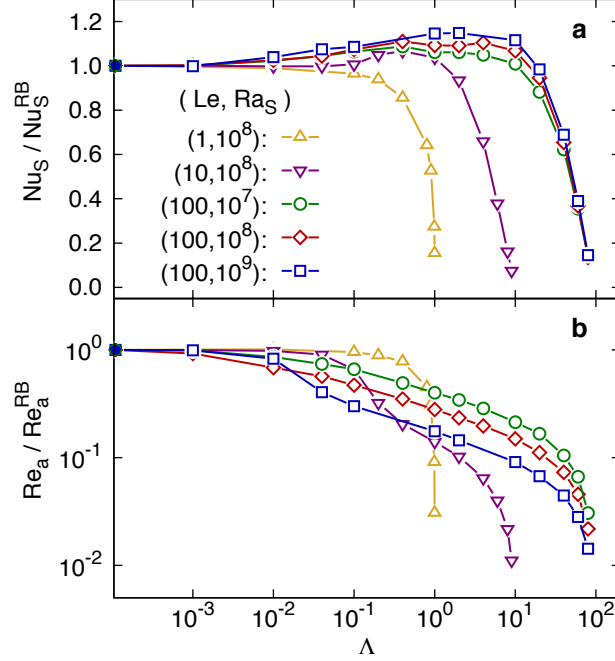


FIG. 3. (a) Salinity flux Nu_S and (b) Reynolds number Re_a versus density ratio Λ for different Lewis numbers and Rayleigh numbers. All quantities are normalized by the values of Rayleigh-Bénard (RB) flow with the same Ra_S and Pr_S . The solid symbols on the vertical axes represent the RB cases within each set. Re_a decreases monotonically for all sets. But Nu_S can be larger than Nu_S^{RB} in the finger regime at $Le > 1$.

exhibit totally different behaviours in the three regimes. In the quasi-RB regime at small Λ both Nu_S and Re_a are very close to Nu_S^{RB} and Re_a^{RB} . As Λ increases, for the four sets with $Le > 1$ Nu_S is larger than Nu_S^{RB} although Re_a decreases according to some effective power-law scaling, which corresponds to the finger regime. When Λ becomes large enough and close to Le , the flow enters the damping regime and both Nu_S and Re_a quickly drop to the values of purely conductive case. For the set with $Le = 1$ the flow directly transits from the quasi-RB regime to the damping regime, thus no increment of Nu_S is found in the whole range of $0 < \Lambda < 1$.

The enhancement of Nu_S in the finger regime is remarkable since we apply a stabilizing temperature field, but nonetheless the salinity transfer is enhanced. Furthermore, the regime with higher salinity flux extends to $\Lambda > 1$ for large Le . Recall that $\Lambda > 1$ corresponds to an overall stable stratification of the fluid. Our results suggest that salinity flux in a stably stratified fluid can exceed that in a unstably stratified state such as purely RB case! For fixed

Le , the increment of Nu_S is more pronounced at higher Ra_S . The highest increment achieved is about 15%, which is comparable to what was found in experiments [24]. However, in our simulations Nu_S follows a trend which is different from the experiment. In experiments Nu_S reaches a maximum at the transition from the quasi-RB to the finger regime, while our results indicate that Nu_S is largest at not the transition but a bigger Λ . The three sets of simulations at $Le = 100$ even suggest that there may exist a range of Λ in the finger regime where Nu_S is nearly constant and larger than the RB value. To clarify this discrepancy more simulations are needed at control parameters similar to those in experiments.

Our previous study [25] suggested that the Grossmann-Lohse (GL) model originally developed for RB flow [12–16] can be directly applied to vertically bounded DDC flow. The prediction of the GL model is consistent with both the numerical data [25] with $Le = 100$ and $\Lambda \in (0.1, 10)$, and the experimental data [22] with $Le \approx 200$ and Λ smaller than or close to 1. Current results indicate that in the quasi-RB regime Nu_S is almost the same as Nu_S^{RB} , and in the finger regime Nu_S is slightly higher than but still quite close to Nu_S^{RB} , thus the GL theory should give good prediction of Nu_S in those two regimes. The largest increment is about 15% for $Le = 100$ and $Ra_S = 10^9$. The Reynolds number, on the other hand, decreases monotonically towards zero as Λ varies from 0 to Le , thus it cannot be predicted by the original GL model. The current numerical results are compared to the GL model for salinity transfer by using the same coefficients as in the pure RB problem [16, 25], see Fig. 4. Only the data in the quasi-RB and finger regimes are included. Note that the GL model is used to predict Nu_S for three different Pr_S values. Indeed the GL model is quite accurate even when shown in the compensated form, which supports our statement that the GL model can be applied to DDC flow, provided that the flow is in the quasi-RB or the finger regime.

The change of flow morphology can be understood by examining the horizontal and vertical velocities separately. Therefore we define a Reynolds number Re_h based on the rms value of the horizontal velocity and a Reynolds number Re_z based on the rms value of the vertical velocity. Similar to Ref. [24] we calculate the ratios of Re_h and Re_z to Re_a , i.e. the ratios of the horizontal and vertical velocities to the total velocity, see Fig. 5. For $Le = 1$ both ratios are nearly constant even for Λ very close to Le . Since Re_a decreases monotonically to zero as Λ approaches Le , the two curves imply that the stabilizing temperature field damps the horizontal and vertical motions simultaneously. When $Le > 1$, however, the two ratios

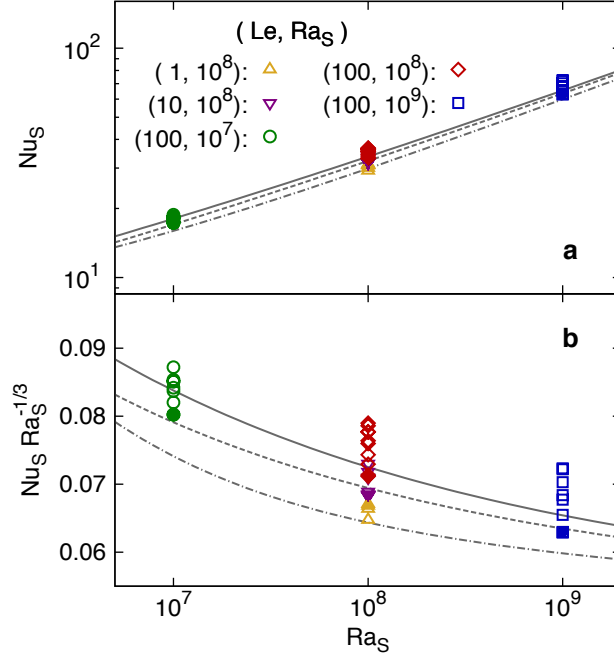


FIG. 4. Comparison between numerical results and the Grossmann-Lohse (GL) theory in their original values (a) and in a compensated way (b). Good agreement can be found between the salinity flux and the GL theory in the quasi-RB and the finger regimes. The GL predictions are shown by the solid line for $Pr_S = 7$, the dashed line for $Pr_S = 70$, and the dash-dotted line for $Pr_S = 700$, respectively.

follow opposite trends. Re_h/Re_a and Re_z/Re_a are constant in the quasi-RB regime with small Λ . When Λ further increases the former decreases to as low as 0.1 and the latter increases to almost 1, implying that the fluid moves mainly in the vertical direction and therefore transfers salinity more efficiently. The domination of vertical velocity marks the onset of the finger regime.

We also show in Fig. 5c the ratio Re_z/Re_h , i.e. the ratio of vertical velocity rms to the horizontal velocity rms. For an isotropic flow this ratio should be $1/\sqrt{2}$. When the vertical and horizontal motions are in balance the ratio is 1. Fig. 5c indicates that in the quasi-RB regime the ratio increases from the isotropic value as Le becomes larger. That is, in our numerical simulations the vertical motion is already stronger than the horizontal one for quasi-RB flows at large Pr_S . This is different from the experimental results [24], where for a much higher Pr_S the flow is still isotropic in the quasi-RB regime. One possible reason may be the different boundary conditions at the side walls. In our simulations periodic boundary

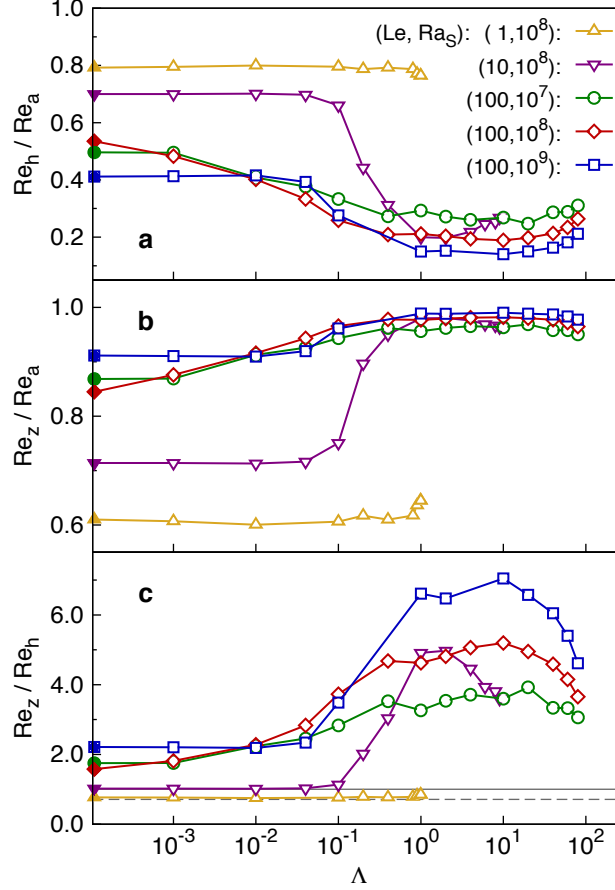


FIG. 5. The ratios between different Reynolds numbers. (a) The ratio Re_h/Re_a between the Reynolds numbers based on the horizontal velocity and the total velocity, (b) the ratio Re_z/Re_a between the Reynolds numbers based on vertical velocity and total velocity, and (c) the ratio between Re_z/Re_h . In (c) the horizontal dashed line marks the isotropic value of $Re_z/Re_h = 1/\sqrt{2}$ and the horizontal solid line $Re_z/Re_h = 1$, respectively. The onset of the finger regime is clearly visible by the breakdown of the horizontal velocity and the increase of the vertical one, or the sudden increase of Re_z/Re_h as shown in (c).

conditions are used for two horizontal directions, while in experiments the side walls are solid and no-slip. Those different horizontal boundary conditions may impose different constraints to the horizontal motions. Nevertheless, for all four sets with $Le > 1$, the ratio Re_z/Re_h experiences a sudden increase at the transition from the quasi-RB to the finger regime. This observation is consistent with experimental results [24], i.e. the transition can be described as a bifurcation.

The results reported here not only reveal some fascinating features about DDC flow for a

wide range of control parameters, but also have great application potentials. For instance, for seawater with $Le \approx 100$ we show that GL model is applicable for Λ up to 10, which covers the common value observed in the main thermocline of the subtropical gyres [2]. Next, transferring scalar component more efficiently in a solution is often desirable in many practical applications. Our results suggest that this can be achieved for a wide range of control parameters, though counterintuitively, by applying a stabilizing thermal gradient to the system. Such enhancement of scalar transfer has been observed in an electrodeposition cell [24].

Appendix A: Methods

We consider an incompressible flow where the fluid density depends on two scalar component and employ the Oberbeck-Boussinesq approximation, i.e. $\rho(\theta, s) = \rho_0[1 - \beta_T\theta + \beta_Ss]$. Here ρ is the fluid density, ρ_0 is a reference density, θ and s are the temperature and salinity relative to some reference values, and β_ζ with $\zeta = T$ or S is the positive expansion coefficient associated to scalar ζ , respectively. The flow quantities include three velocity components u_i with $i = 1, 2, 3$, the pressure p , and two scalars θ and s . The governing equations read

$$\partial_t u_i + u_j \partial_j u_i = -\partial_i p + \nu \partial_j^2 u_i + g_i(\beta_T \theta - \beta_S s), \quad (\text{A1a})$$

$$\partial_t \theta + u_j \partial_j \theta = \kappa_T \partial_j^2 \theta, \quad (\text{A1b})$$

$$\partial_t s + u_j \partial_j s = \kappa_S \partial_j^2 s, \quad (\text{A1c})$$

where ν is the kinematic viscosity, g_i is the constant acceleration of gravity, and κ_ζ is the diffusivity of scalar ζ , respectively. The dynamic system is further constrained by the continuity equation $\partial_i u_i = 0$. Without loss of generality, we set $g_1 = g_2 = 0$ and $g_3 = g$.

The flow is vertically bounded by two parallel plates separated by a distance L . The plates are perpendicular to the direction of gravity. At two plates the no-slip boundary condition is applied, i.e. $u_i \equiv 0$, and both scalars are kept constant. The top plate has higher temperature and salinity, thus the flow is driven by the salinity difference Δ_S across two plates and stabilized by the temperature difference Δ_T . In the two horizontal directions we employ the periodic boundary condition. The horizontal box size is set to be much larger than the horizontal length scales of the flow structures. Initially velocity is set at zero, temperature has a vertically linear profile, and salinity is uniform and equal to the average

of boundary values at two plates. The initial fields are similar to those in experiments [22]. In order to accelerate the flow development, random noise with a relative amplitude of 0.1% is added to temperature and salinity field. Such initial conditions are used in all simulations.

Equation A1 is nondimensionalized by using the length L , the free-fall velocity $U = \sqrt{g\beta_S\Delta_S L}$, and the scalar differences Δ_T and Δ_S . To numerically solve the equations we utilised a finite difference solver [26] together with a highly efficient multi-resolution technique [27]. The numerical method has been validated by one-to-one comparisons with experimental results [25].

ACKNOWLEDGMENTS

This study is supported by Stichting FOM and the National Computing Facilities, both sponsored by NWO, the Netherlands. The simulations were conducted on the Dutch super-computer Cartesius at SURFsara.

-
- [1] J. Turner, *Multicomponent convection*, Annu. Rev. Fluid Mech., 17 (1985), pp. 11–44.
 - [2] R.W. Schmitt, *Double diffusion in oceanography*, Annu. Rev. Fluid Mech., 26 (1994), pp. 255–285.
 - [3] R.W. Schmitt, J.R. Ledwell, E.T. Montgomery, K.L. Polzin and J.M. Toole, *Enhanced diapycnal mixing by salt fingers in the thermocline of the tropical Atlantic*, Science, 308 (2005), pp. 685–688.
 - [4] S. Schoofs, F.J. Spera, and U. Hansen, *Chaotic thermohaline convection in low-porosity hydrothermal systems*, Earth Planetary Sci. Lett., 174 (1999), pp. 213–229.
 - [5] B.A. Buffett, and C.T. Seagle, *Stratification of the top of the core due to chemical interactions with the mantle*, J. Geophys. Res.: Solid Earth, 115 (2010), B04407.
 - [6] W. Merryfield, *Hydrodynamics of semiconvection*, Astrophys. J., 444 (1995), pp. 318–337.
 - [7] E. Rosenblum, P. Garaud, A. Traxler, and S. Stellmach, *Turbulent mixing and layer formation in double-diffusive convection: Three-dimensional numerical simulations and theory*, Astrophys. J., 731 (2011), 66.
 - [8] J. Leconte, and G. Chabrier, *A new vision of giant planet interiors: Impact of double diffusive*

- convection*. A&A, 540 (2012), A20.
- [9] G.M. Mirouh, P. Garaud, S. Stellmach, A.L. Traxler, and T.S. Wood, *A new model for mixing by double-diffusive convection (semi-convection). I. the conditions for layer formation*. Astrophys. J., 750 (2012), 61.
 - [10] T.S. Wood, P. Garaud, and S. Stellmach, *A new model for mixing by double-diffusive convection (semi-convection). II. the transport of heat and composition through layers*. Astrophys. J., 768 (2013), 157.
 - [11] J. D’Hernoncourt, A. Zebib, and A. De Wit, *Reaction driven convection around a stably stratified chemical front*. Phys. Rev. Lett., 96 (2006), 154501.
 - [12] S. Grossmann, and D. Lohse, *Scaling in thermal convection: a unifying theory*. J. Fluid Mech., 407 (2000), pp. 27–56.
 - [13] S. Grossmann, and D. Lohse, *Thermal convection for large Prandtl numbers*. Phys. Rev. Lett., 86 (2001), pp. 3316–3319.
 - [14] S. Grossmann, and D. Lohse, *Prandtl and Rayleigh number dependence of the Reynolds number in turbulent thermal convection*. Phys. Rev. E, 66 (2002), 016305.
 - [15] S. Grossmann, and D. Lohse, *Fluctuations in turbulent Rayleigh-Bénard convection: The role of plumes*. Phys. Fluids, 16 (2004), pp. 4462–4472.
 - [16] R.J.A.M. Stevens, E.P. van der Poel, S. Grossmann, and D. Lohse, *The unifying theory of scaling in thermal convection: the updated prefactors*. J. Fluid Mech., 730 (2013), pp. 295–308.
 - [17] T. Radko, *Double-diffusive convection*, Cambridge University Press, Cambridge, UK, (2013).
 - [18] M.E. Stern, *The Salt-Fountain and thermohaline convection*, Tellus, 12 (1960), pp. 172–175.
 - [19] J. Turner, *Salt fingers across a density interface*, Deep Sea Res., 14 (1967), pp. 599–611.
 - [20] P.F. Linden, *The formation of banded salt finger structure*. J. Geophys. Res.: Oceans, 83 (1978), pp. 2902–2912.
 - [21] R. Krishnamurti, *Double-diffusive transport in laboratory thermohaline staircases*. J. Fluid Mech., 483 (2003), pp. 287–314.
 - [22] E. Hage, and A. Tilgner, *High Rayleigh number convection with double diffusive fingers*. Phys. Fluids, 22 (2010), 076603.
 - [23] R.W. Schmitt, *Thermohaline convection at density ratios below one: A new regime for salt fingers*. J. Marine Res., 69 (2011), pp. 779–795.
 - [24] M. Kellner, and A. Tilgner, *Transition to finger convection in double-diffusive convection*.

- Phys. Fluids, 26 (2014), 094103.
- [25] Y. Yang, E.P. van der Poel, R. Ostilla-Mónico, C. Sun, R. Verzicco, S. Grossmann, and D. Lohse *Salinity transfer in bounded double diffusive convection*. J. Fluid Mech., 768 (2015), pp. 476–491.
- [26] R. Verzicco, and P. Orlandi, *A finite-difference scheme for three-dimensional incompressible flow in cylindrical coordinates*. J. Comput. Phys., 123 (1996), pp. 402–413.
- [27] R. Ostilla-Mónico, Y. Yang, E.P. van der Poel, D. Lohse, and R. Verzicco, *A multiple-resolution strategy for Direct Numerical Simulation of scalar turbulence*. J. Comput. Phys., 301 (2015), pp. 308–321.